Journal of Low Temperature Physics (2026) 222:27
https://doi.org/10.1007/s10909-025-03361-9

Development of Cryogenic X-Ray Detectors Based on Mo/Au TES

A. Camón[1] · L. Fàbrega[2] · C. Pobes[1] · P. Strichovanec[1] · J. Bolea[3] · J. I. Rico-Camacho[1] · J. L. García-Palacios[1]

Received: 24 September 2025 / Accepted: 22 December 2025

Abstract
Transition edge sensors (TESs) have emerged as highly sensitive radiation detectors with applications ranging from astrophysics to materials science. In the framework of the Athena X-ray space telescope, we have developed Mo/Au-based TES devices designed to meet the ESA specifications for the X-IFU instrument. The detectors were fabricated using a Mo/Au/Au trilayer process and characterized in a dilution refrigerator using a SQUID readout. From I to V curves and complex impedance measurements, we extracted the electrothermal parameters of the TES, which are consistent with theoretical models. Noise spectra were analyzed to estimate the energy resolution, and an excess noise factor was obtained from the comparison of theoretical and experimental data. A spectral resolution below 4 eV was achieved for 5.9 keV X-rays from a ^{55}Fe source.

Keywords Cryogenic detectors · Superconductivity · Transition edge sensors

1 Introduction

Since K. D. Irwin proposed their use under voltage bias in 1995 [1], microcalorimeters based on transition edge sensors (TESs) have become one of the best radiation detectors available. Depending on their design and the absorber material used, they are able to detect individual photons across a wide range of frequencies, from microwaves to gamma-rays, with exceptional spectral resolution [2]. Moreover, they exhibit extremely low dark count rates. TES devices are nowadays employed

---

A. Camón
acamon@unizar.es

[1] Instituto de Nanociencia y Materiales de Aragón (INMA), CSIC-Universidad de Zaragoza, 50009 Zaragoza, Spain

[2] Institut de Ciència de Materials de Barcelona (ICMAB-CSIC), Campus de Bellaterra, 08193 Bellaterra, Spain

[3] Centro Universitario de la Defensa, Zaragoza, Spain

in a variety of fields, including astrophysics and materials science [3]. One notable upcoming application is the Athena mission [4], an X-ray space telescope to be launched by the European Space Agency (ESA) in the oncoming decade.

Several groups, such as SRON [5], NIST [6], and NASA [7], have already developed detectors that meet the Athena mission specifications, achieving energy resolutions better than 2 eV at 7 keV. Our group has been developing TES devices with the Athena requirements in mind for more than a decade. We are currently also developing devices for other applications within the same energy range (synchrotron facilities and axion searches). In this work, we summarize the main milestones achieved by our group to date. Section 2 describes the detector fabrication process, Sect. 3 presents the characterization system, and Sect. 4 shows selected results for a representative device.

2 Fabrication

For our devices, 4-inch, 525-µm-thick silicon wafers with 500-nm-thick low stress Si_3N_4 layer in both sides are used as substrate. To avoid problems associated with Mo oxidation, when the sample is transferred between the sputtering system and the e-beam during the fabrication process, our group developed the trilayer solution [8], combining magnetron sputtering and e-beam deposition. We use a magnetron AJA Orion 5 UHV sputtering system and an e-beam PVD system Edwards 500 UHV. First, the 45 nm of Mo layer is deposited by using radio frequency (RF) power supply from a 2-inch diameter Mo target of 99.95% purity. Then, a 15-nm protective Au layer is deposited by direct current (DC) power supply from a 2-inch-diameter Au target of 99.99% purity. The Ar working pressure is fixed to 3 mTorr. The deposition rates are 9 nm/min for Mo and 10 nm/min for Au. Afterward, the wafer is taken out from the sputtering chamberand loaded into the e-beam evaporation system, where 250 nm of high purity (99.99%) Au is evaporated (rate of 10 nm/min). These Mo and Au thicknesses determine a superconducting critical temperature close to 100 mK via the proximity effect [9].

After finishing the trilayer deposition, the Si_3N_4 membranes on the back side of the wafer are defined by using optical lithography (K.Suss MA6 aligner) with positive photoresist AZ ECI 3027. The size of the aperture in the Si_3N_4 backside layer is calculated for anisotropic wet etching of (100) silicon in KOH solution to reach the correct size of membrane on the top side of the wafer. Then, Si_3N_4 is etched away by reactive ion etching (RIE) with SF_6 plasma.

Positive resin lithography (AZ ECI 3027) is used to define the area of the thermometer (Mo/Au/Au). The combination of ion milling (IM) and RIE allows etching away the Au and partially the Mo layer, where approximately 10 nm of Mo layer is left. After resin cleaning, 150 nm of Nb is deposited by DC sputtering with the rate 7.5 nm/min at a pressure 3 mTorr of Ar. Before Nb deposition, the surface is cleaned by RF bias Ar plasma in the same chamber. This step allows to remove all surface contamination and produces a clean interface between Mo and Nb. Next, the Nb paths are defined with positive photoresist (AZ ECI 3027). The RIE (CF_6 plasma) is used to etch away the Nb and the rest of the Mo layer.

After removal of the remaining photoresist, a two-level lithography process is carried out for the fabrication of a cantilevered X-ray absorber. First, the positive photoresist (AZ ECI 3027) is used to define 2.5-μm stems that support the absorber on the Si_3N_4 membrane, and produce a thermal contact point to the Mo/Au thermometer. Then, a Ti/Au (5/100 nm) seed layer is evaporated on, forming a bottom contact for plating. The area of absorber is defined by a second lithography using 7-μm-thick positive photoresist (AZ XT10), being later exposed for plating.

A homemade electrochemical cell supplied by an AUTOLAB PGSTAT12 potentiostat is used for Au plating. This method permits deposition of high purity Au (RRR = 35) of few micrometers thickness. Three-electrode system consists of a Pt counter-electrode (CE), an Ag/AgCl reference electrode, and a working electrode (WE). The WE is the 4″ wafer with the Au seed layer and chips distribution defined by lithography to open a total area of 10 cm^2. A commercial solution, TECHNI GOLD 25 ES is used for Au plating. The 2.5-μm Au layer is deposited by applying a constant current mode with the solution heated to 55 °C. The current is set to 1.2 mA/cm^2 providing a deposition rate of 75 nm/min, that allows to deposit a bright and flat Au gold layer. After deposition, the wafer is rinsed with deionized water and dried by N_2. In some cases, to increase the quantum efficiency of the absorber, an additional layer of Bi is deposited using a commercial plating solution, NB 100 (NB Technologies), in an electrochemical cell dedicated exclusively to Bi. A constant current of 2.5 mA/cm^2 at room temperature provides a deposition rate of approx. 80 nm/min to reach a typical thickness between 3 and 5 μm.

After cleaning the upper thick photoresist, the seed layer is etched off by IM. Finally, the bottom photoresist is dissolved and cleaned by acetone, isopropanol, and ethanol bath. To release the Si_3N_4 membranes, the Si substrate is wet etched selectively by 40% KOH solution at 80 °C. To protect the top side of the wafer, where the TES are, the wafer is hermetically closed into the PEEK wafer chuck, and only the backside of the wafer is exposed for wet etching.

Up to 32 (10 × 10 mm) chips are usually distributed in every 4″ wafer. This allows for a wide variety of designs to be tested, from bilayer geometry or absorber coupling in single pixels, to arrays. Figure 1 shows a schematic cross-section of a typical single pixel.

TES devices with different geometries, sizes, and absorber stem position have been designed and fabricated. An example of a representative TES, developed to achieve the best energy resolution in accordance with the specifications of the X-IFU instrument, is presented in Fig. 2.

3 Characterization Setup

Figure 3 shows a schematic of the circuit used for the TES characterization. When a photon is absorbed, the TES heats up, and since it is biased within the superconducting transition, its resistance changes sharply. This leads to a change in the current flowing through the SQUID's pickup coil. The SQUID detects this

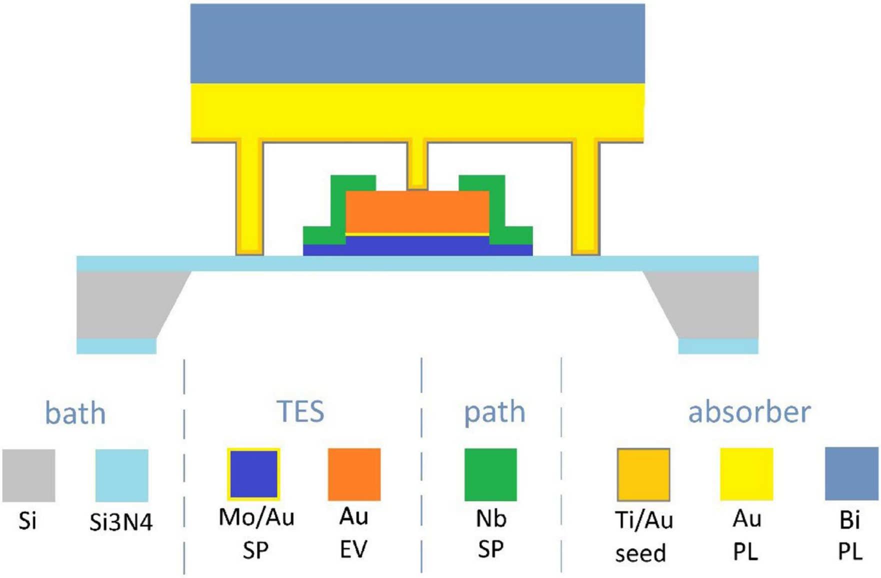

Fig. 1 Schematic cross-section of a TES with absorber (SP: sputtering, EV: e-beam evaporation, PL: plating)

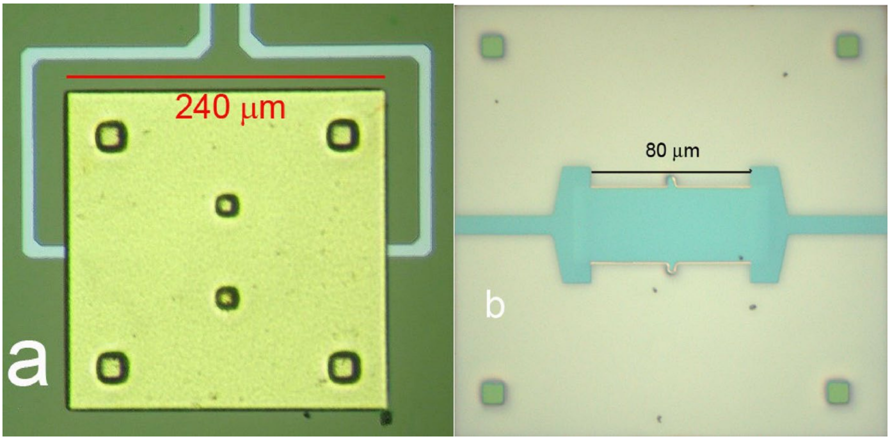

Fig. 2 Optical micrographs of a TES. **a** Top-view image of a TES showing the Au absorber (240 × 240 μm), two central stems tangent to the edge of the trilayer, and four outer stems laying on the membrane. Mo/Nb paths with a width of 15 μm can also be seen. **b** Bottom view of the same detector through the membrane, showing the TES sensor in addition to the absorber stems and the paths

variation and converts it into a voltage pulse. The SQUID used is a dual-channel model C6_X226LB provided by PTB (Berlin). It also includes the shunt resistor (R_{shunt}), which in our case is of 2 mΩ. An encapsulated ^{55}Fe source, mounted directly above the TES, is eventually used as the X-ray source. The full setup

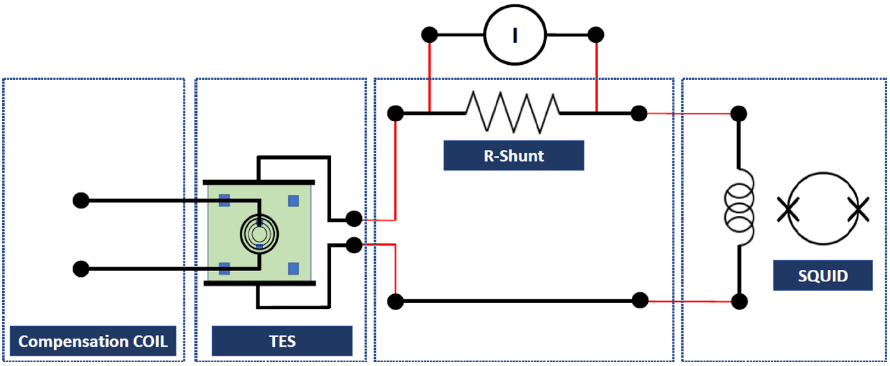

Fig. 3 Circuit scheme used for TES characterization

is hosted in a Bluefors dilution refrigerator, achieving a base temperature below 10 mK.

TESs are highly sensitive to magnetic fields. For this reason, the entire holder is magnetically shielded using a superconducting aluminum enclosure and a CRYOPERM shield. If any residual field remains, B_{res}, it is compensated by using a superconducting Helmholtz coil placed at the sample holder, ensuring that the TES operates in a nearly zero-field environment. To estimate $\mathrm{B}_{\mathrm{res}}$, we bias the TES within its transition region and sweep the applied magnetic field to maximize the SQUID output. B_{res} rarely exceeds 0.6 µI.

To minimize external noise, the power line is filtered through an ultra-isolation transformer and an uninterruptible power supply (UPS). To avoid ground loops, optical fiber connections are used. A low-noise differential preamplifier (Stanford Research Systems SR560) is used to set the bandwidth and conditioning the signal from the SQUID. Finally, a 24-bit NI PXI-5922 digitizer is used to acquire voltage pulses generated by the arrival of X-ray photons at the detector.

By using this setup, several measurements are performed to fully characterize the detector. I–V curves are acquired with a HP 3458A multimeter at different bath temperatures, T_{bath} (Fig. 4), from which the TES thermal parameters are extracted (n, K, T_0, and G) [10]. A Hewlett-Packard HP 3562A spectrum analyzer is used to perform complex impedance measurements (Fig. 5). We estimate the electrical parameters: α, β (logarithmic derivatives of $R(T,I)$), τ_I, and heat capacity C [11] based on a one thermal block model (1 TB) [12]. τ_I is defined in [12] Eq. 18. The noise performance parameters are also estimated [12].

4 Results

The characterization results of a representative TES are presented below. Assuming a 1 TB model $P_{\mathrm{bath}} = P_{\mathrm{joule}}$, by fitting the set of I–V curves at different bath temperatures (Fig. 6) to the expression:

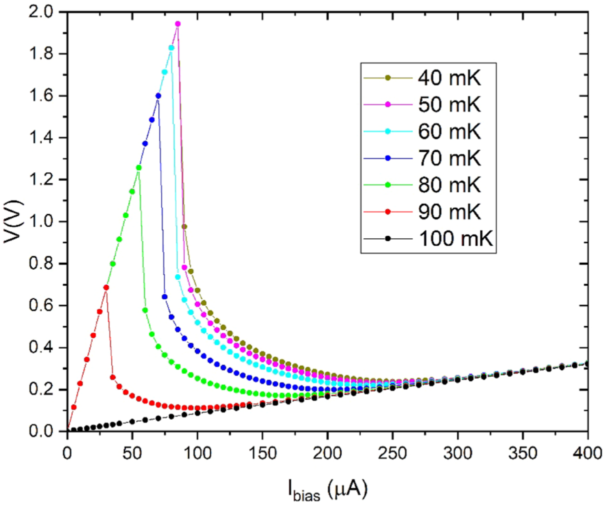

Fig. 4 A set of I–V curves at different T_{bath}, from 40 to 100 mK

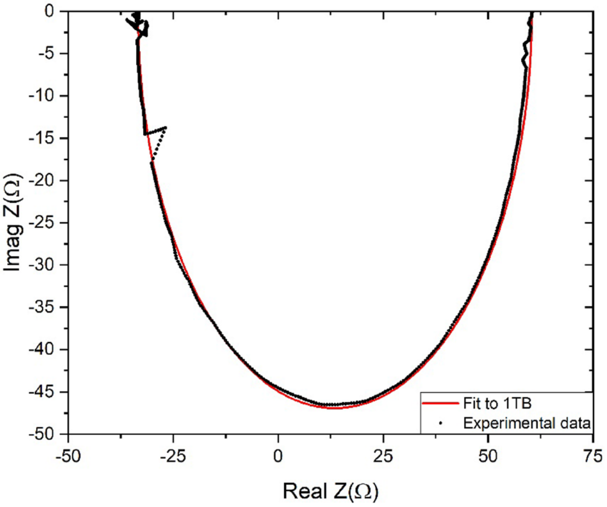

Fig. 5 Imag. versus Real plot of the AC impedance taken at 50% Rn and $T_{\mathrm{bath}} = 50$ mK. In red the fit to 1 TB. The spikes in the curve are due to pulses caused by X-ray photons from the ^{55}Fe source

$$P_{\mathrm{bath}} = K\left(T_0^n - T_{\mathrm{bath}}^n\right)$$

the thermal parameters of the TES (*n, K, G,* and T_0) are obtained [10], as summarized in Table 1. The *n* value of 3.5 is in good agreement with the calculations reported by Anghel et al. [13].

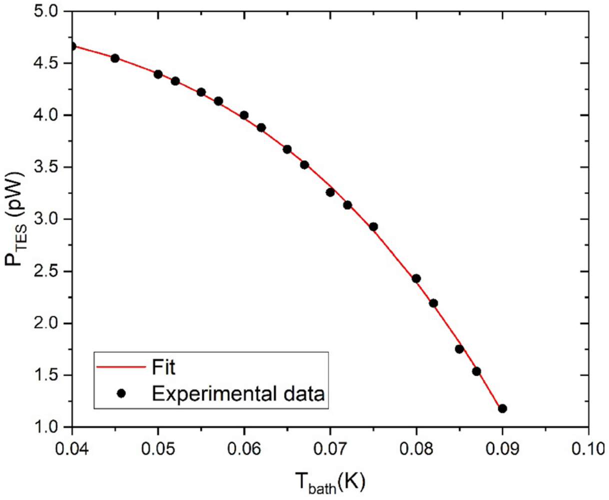

Fig. 6 Power-law fit of the I–V curves at different temperatures taken al 80%Rn. From this fit, the thermal parameters (n, k, G, and T_0) are computed

Table 1 TES parameters

Length	80 µm
Width	40 µm
T_0 (50%Rn)	94 mK
Rn	60 mΩ
n	3.5 ± 0.2
G (20%Rn)	156 ± 10 pW/K
C (20%Rn)	1.5 ± 0.1 pJ/K
α (20%Rn)	300 ± 10
β (20%Rn)	2.3 ± 0.1
L	57 nH
τ_I(20%Rn)	145 ± 1 µs

Electrical parameters of the TES (α, β, τ_I and C and C) are derived by fitting [11] the complex impedance data at different bias points to a 1 TB model [12] (see Table 1).

The TES energy resolution can be estimated from the experimental noise spectrum ($\Delta E_{\mathrm{baseline}}$) and also from the theoretical noise spectrum (ΔE_{th}), both based on the noise model (Figs. 7 and 8).

In both cases, the definition follows Eq. (97) from [12] although the integral bandwidth is restricted between 10 Hz and 100 kHz.

$$\Delta E_{\mathrm{FWHM}} = \frac{2\sqrt{2Ln(2)}}{\sqrt{\int_0^\infty \frac{4}{\mathrm{NEP}(\omega)^2} d\omega}}$$

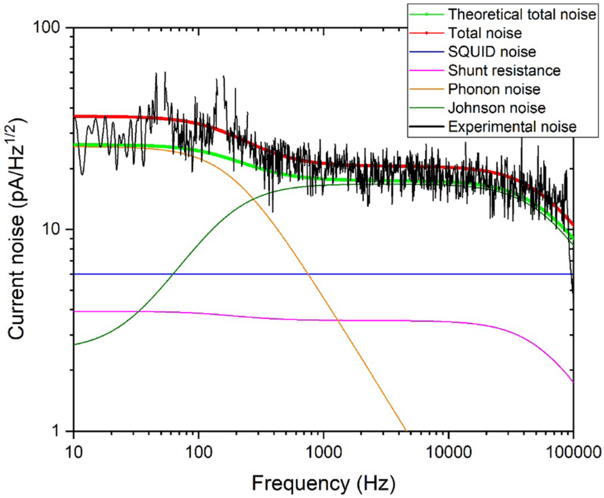

Fig. 7 Experimental noise spectrum of the TES measured at a bias point of 30% Rn and a bath temperature of 50 mK. The theoretical total noise is obtained by summing up all individual noise contributions. To account for the observed excess noise, the Johnson noise is scaled by a factor of $(1+M^2)$ and the phonon noise by $(1+M_{\mathrm{ph}}{}^2)$. The noise components were calculated using the TES parameters extracted from the I–V curves and the complex impedance based on a 1 TB model

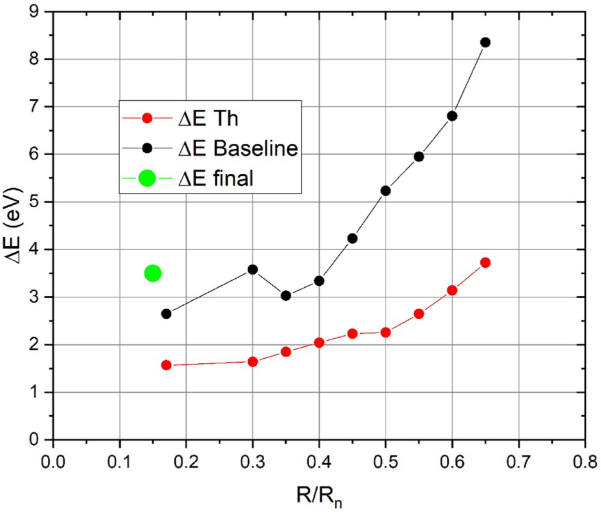

Fig. 8 ΔE_{Th} and $\Delta E_{\mathrm{baseline}}$ as a function of R/Rn. For a typical operating point of 0.15, the ΔE_{Th} is approximately 1.5 eV, while the $\Delta E_{\mathrm{baseline}}$ is around 2.7 eV and $\Delta E_{\mathrm{final}}$ is 3.5 eV

From the difference between the theoretical and experimental noise, the excess noise parameter M^2 is estimated (Fig. 9). The figure shows the relationship between M^2 and α for this device which remains approximately constant, $M^2/\alpha = 0.005$. This result is consistent with those reported in [14]. This relation implies that TESs with

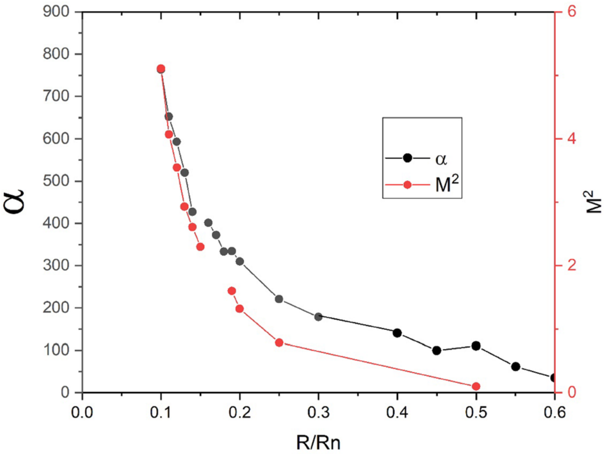

Fig. 9 Excess-noise parameter, M^2, and α as a function of R/Rn

a larger α do not necessarily achieve better energy resolution, as it is often associated with higher M^2 values. Therefore, a trade-off between both parameters is required.

Finally, Fig. 10 shows a histogram from the acquisition of 1730 pulses, yielding a final spectral resolution ($\Delta E_{\mathrm{final}}$) of 3.5 ± 0.2 eV for the Kα complex of the ^{55}Fe source (5.9 keV). The discrepancy between $\Delta E_{\mathrm{final}}$ and $\Delta E_{\mathrm{baseline}}$ may suggest that the intrinsic resolution of the devices is already at the state of the art and that the measured final resolution is being limited by a setup contribution. We are working on improving temperature stability and vibration isolation to reduce this contribution.

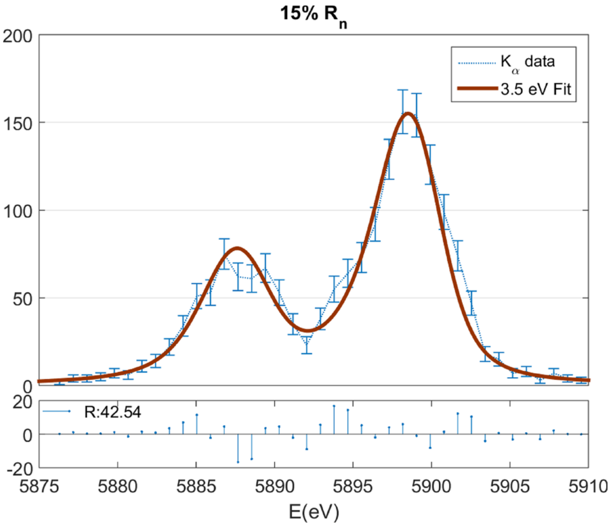

Fig. 10 Spectrum of ^{55}Fe Kα lines obtained with the pixel in Fig. 2. at 15% of Rn

A detailed analysis of the effect of T_{bath} on the resolution at low operating point will be presented elsewhere.

5 Conclusions and Outlook

We are developing Mo/Au-based TES X-ray detectors, focusing on the specifications defined by ESA for the X-IFU instrument of the Athena mission. We have developed fabrication and full characterization setups and have designed, fabricated, and characterized many devices. In this paper, we presented the best results achieved so far. Energy resolutions below 4 eV have been obtained, possibly limited by experimental setup contributions. Further improvements are currently being developed, including better temperature stability, a new anti-vibration system and an optimization of the circuit inductance (L). These upgrades are expected to enable further enhancement of the achieved energy resolution.

Although this manuscript presents only the results of a representative TES for X-IFU, different TES have been developed to perform a broad range of studies. For instance, in [15], the physical origin of the superconducting transition was investigated; in [16], the temperature and current sensitivities of bare Mo/Au TES were analyzed; and in [17], the proximity effect in Mo/Au TES was explored.

Ongoing work is currently focused on the optimal choice of the operating point and on the influence of TES design on fundamental parameters and excess noise as well as on the development of TES for other applications.

Acknowledgements The Spanish ”Ministerio de Ciencia, Innovación y Universidades” supports and funds this works, MICIU/AEI/https://doi.org/10.13039/501100011033 under Grants No. PID2021-122955OB-C42 (also funded by FEDER, UE), No. PID2024-155779OB-C32, No. CEX2023-001286-S (Severo Ochoa Centers of Excellence). We also acknowledge the Aragón Regional Government through project QMAD (E09 23R). LF acknowledges also Spanish MICINN for support through the Severo Ochoa Programme for Centres of Excellence (project MATRANS42, CEX2023-001263-S). We also acknowledge PTB (Berlin) for providing us with excellent SQUIDs, and Jörn Beyer for his valuable help and advice.

Author's Contribution A.C. wrote the main manuscript text and prepared Figs. 4–8. P.S. prepared Figs. 1–2. J.I.R. prepared Fig. 3. C. P. prepared Fig. 9. All authors reviewed the manuscript.

Funding Open Access funding provided thanks to the CRUE-CSIC agreement with Springer Nature.

Data Availability The data that support these findings are available from the corresponding author upon reasonable request.

Declarations

Conflict of interest The authors declare no competing interests.

References

1. K.D. Irwin, Appl. Phys. Lett. **66**, 1998 (1995). https://doi.org/10.1063/1.113674
2. J.N. Ullom, D.A. Bennett, Supercond. Sci. Technol. **28**, 084003 (2015). https://doi.org/10.1088/0953-2048/28/8/084003
3. L. Gottardi, K. Nagayashi, Appl. Sci. **11**, 3793 (2021). https://doi.org/10.3390/app11093793
4. D. Barret, V. Albouys, Jan-Willem den Herder, L. Piro, et al. Exp. Astron. (2023). https://doi.org/10.1007/s10686-022-09880-7
5. M. de Wit, L. Gottardi, K. Nagayoshi, H. Akamatsu, M. P. Bruijn, M. L. Ridder, E. Taralli, D. Vaccaro, J.R. Gao, J.W.A. den, Proc. SPIE 12181, Space Telescopes and Instrumentation (2022). https://doi.org/10.1117/12.2629368
6. J. C. Weber, K.M. Morgan, D. Yan, C.G. Pappas, A.L. Wessels, G. C. O. Neil, D.A. Bennett, G. c. Hilton, D. S. Swetz, J. N. Ullom, D. R. Schmidt, Supercond. Sci.and Technol. **33** 115002. (2020) https://doi.org/10.1088/1361-6668/abb206
7. N.A. Wakeham, S.J. Adams, S.R. Bandler, S. Beaumont, J.A. Chervenak, R.S. Cumbee, F.M. Finkbeiner, J.Y. Ha, S. Hull, R.L. Kelley, C.A. Kilbourne, F.S. Porter, K. Sakai, S.J. Smith, E.J. Wassell, S. Yoon, IEEE Trans. Appl. Supercond. **33**, 1–6 (2023). https://doi.org/10.1109/TASC.2023.3253067
8. L. Fàbrega, I. Fernández, O. Gil, M. Parra-Borderías, A. Camón, R González, J. Sesé, F. Briones. IEEE Trans. Appl. Supercon. **19**, 460 (2009) https://doi.org/10.1109/TASC.2009.2019052
9. J.M. Martinis, G.C. Hilton, K.D. Irwin, D.A. Wollman, Nucl. Instrum. Methods Phys. Res. Sect. A Accel. Spectrom. Detect. Assoc. Equip. **444**, 23 (2000)
10. T. Saab, E. Apodacas, S.R. Bandler, K. Boyce, J. Chevernak, E. Figueroa-Feliciano, F. Finkbeiner, C. Hammock, R. Kelley, M. Lindeman, F.S. Porter, C.K. Stahle, Nucl. Instr. And Meth. A **520**, 281 (2004)
11. M. A. Lindeman, S. Bandler, R. G. Brekosly, J. A. Chevernak, E. Figueroa-Feliciano, F. M. Finkbeiner, M. J. Li, C.A. Kilbourne, M. Rev. Sci. Instrum. **75**, 1283 (2004) https://doi.org/10.1063/1.1711144
12. K. D.Irwin, G. C.Hilton, in Enss C. (eds.) Cryogenic particle detection, Topics in Appl. Phys. 99, Springer, Berlin, pp 63–150 (2005)
13. D.V. Anghel, C. Caraiani, Y.M. Galperin, Phys. Scr. **94**, 105704 (2019). https://doi.org/10.1088/1402-4896/ab2346
14. N. A. Wakeham, J.S. Adams, S.R. Bandler. S. Beaumont, J. A. Chervenak, A. M. Datesman, M. E. Eckart, F. M. Finkbeiner, R. Hummatov, R. L. Kelly, C. A. Kilbourne, A. R. Miniussi, F. S. Porter, J. E. Sadleir, K. Sakai, S. L. Smith, E. J. Wassell, J. Appl. Phys. **125**, 164503 (2019) https://doi.org/10.1063/1.5086045
15. L. Fàbrega, A. Camón, C. Pobes, P. Strichovanec, J. Appl. Phys. **136**, 154503 (2024). https://doi.org/10.1063/5.0225871
16. L. Fàbrega, A. Camón, C. Pobes, P. Strichovanec, J. Bolea, M. Mas, J. Low Tem. Phys. (2022). https://doi.org/10.1007/s10909-022-02721-0
17. L. Fàbrega, A. Camón, C. Pobes, P. Strichovanec, IEEE Trans. Appl. Supercon. **29**, 2100405 (2019). https://doi.org/10.1109/TASC.2019.2903994